Nano Research
2019, 12(6): 1417–1422

ISSN 1998-0124 CN 11-5974/O4
https://doi.org/10.1007/s12274-019-2366-z

Research Article

"Chameleon-like" optical behavior of lanthanide-doped fluoride nanoplates for multilevel anti-counterfeiting applications

Wenwu You, Datao Tu (✉), Renfu Li, Wei Zheng, and Xueyuan Chen (✉)

CAS Key Laboratory of Design and Assembly of Functional Nanostructures, and Fujian Key Laboratory of Nanomaterials, Fujian Institute of Research on the Structure of Matter, Chinese Academy of Sciences, Fuzhou 350002, China

Received: 29 December 2018 / **Revised:** 26 February 2019 / **Accepted:** 2 March 2019

ABSTRACT

Lanthanide-based luminescent anti-counterfeiting materials are widely used in various kinds of products. However, the emission color of traditional lanthanide-based luminescent materials usually remains nearly unaltered upon different excitation lights, which may only work for single-level anti-counterfeiting. Herein, the $NaYbF_4$:2%Er@$NaYF_4$ core/shell nanoplates (NPs) with "chameleon-like" optical behavior are developed. These NPs display single-band red or green downshifting (DS) emission upon excitation at 377 or 490 nm, respectively. Upon 980 nm excitation, the color of upconversion (UC) emission can be finely tuned from green to yellow, and to red with increasing the excitation power density from 0.1 to 4.0 W/cm^2. The proposed materials readily integrate the advantages of excitation wavelength-dependent DS single-band emissions and sensitive excitation power-dependent UC multicolor emissions in one and the same material, which has never been reported before. Particularly, the proposed NPs exhibit excellent performance as security labels on trademark tag and security ink on painting, thus revealing the great potential of these lanthanide-doped fluoride NPs in multilevel anti-counterfeiting applications.

KEYWORDS

lanthanide-doped, chameleon-like, upconversion, downshifting, multilevel anti-counterfeiting

1 Introduction

Counterfeiting of paper money, medicine, valuable documents, certificates, and famous-brand products is currently a bothersome issue in the world [1–3]. In order to prevent counterfeiting, many anti-counterfeiting strategies such as barcodes, watermarks, holograms, and fluorescent anti-counterfeiting are developed [3]. Among them, fluorescent anti-counterfeiting materials receive great attention and are widely used in various kinds of products due to its low cost and high discrimination ability [4]. As an important kind of phosphors, lanthanide-based luminescent materials show unique physicochemical and optical properties, such as low toxicity, long-lived luminescence, large antenna-generated Stokes or anti-Stokes shifts, narrow emission bands, high resistance to photobleaching, good chemical stability, and color-tunable emissions. These properties render lanthanide-based luminescent materials ideal for anti-counterfeiting applications [5–9].

Generally, there are two main types of photoluminescence (PL) for lanthanide-based materials: downshifting (DS) and upconversion (UC) [10–12]. DS is the process of absorbing higher-energy photons and then emitting lower-energy photons. UC, which is contrary to DS, can convert the lower-energy photons to higher-energy photons through successive absorption of two or more photons. Due to their unique and abundant energy level structures, lanthanide ions usually exhibit multicolor emissions from ultraviolet (UV) to visible, and to near-infrared (NIR) [13, 14]. However, most of the lanthanide-based anti-counterfeiting materials only can display nearly unchanged color upon different excitation lights. Although these materials are well suited for single-level anti-counterfeiting, the fluorescent labels made by these materials can be easily imitated by utilizing other substitutes with similar emission. Thus, developing multilevel anti-counterfeiting materials that show "chameleon-like" optical behavior is highly in demand.

In the past years, lanthanide-doped fluoride nanocrystals (NCs) have attracted extensive attention due to their high DS luminescence (DSL) and UC luminescence (UCL) efficiency [15–26]. In order to realize multicolor emissions, several strategies have been explored [27–30]. For example, our group previously synthesized lanthanide doped $KGdF_4$ NCs, which exhibited red, green, and blue color via doping with Eu^{3+}, Tb^{3+}, and Dy^{3+} ions, respectively [31]. Zhang and co-workers reported that the UCL color can be manipulated in $NaGdF_4$:Yb/Tm/Er@$NaGdF_4$:Eu@$NaYF_4$ NCs by changing the excitation power density from 3 to 30 W/cm^2 [27]. Similarly, Wang and co-workers reported that the red-to-green (*R*/*G*) UC emission intensity ratio of $NaYF_4$@$NaYF_4$:Yb/Ho@$NaYF_4$ NCs can be tuned from 0.37 to 5.19 by increasing the excitation power density from 1.25 to 46.25 W/cm^2 [28]. It should be noted that complicate structure design or very high excitation power density are generally required to achieve tunable multicolor emissions, thus limiting their practical applications.

In this work, we report a promising candidate of multilevel anti-counterfeiting materials based on "chameleon-like" $NaYbF_4$:2%Er@$NaYF_4$ core/shell nanoplates (NPs). The as-prepared NPs feature single-band red or green emissions upon excitation at 377 or 490 nm, respectively. Besides, the as-prepared NPs show very bright UC emission upon 980-nm excitation with UC quantum yield (UCQY) of 5.2%. As a result of efficient energy transfer between Yb^{3+} and Er^{3+} ions, their UCL color is very sensitive to the excitation power density. The *R*/*G* ratio can be tuned from 1.2 to 13.5 when the excitation power density increased from 0.1 to 4.0 W/cm^2. Correspondingly,

Address correspondence to Datao Tu, dttu@fjirsm.ac.cn; Xueyuan Chen, xchen@fjirsm.ac.cn

the displayed UCL color can be finely tailored from green to yellow and to red. Moreover, their PL mechanism is systematically investigated in order to clarify the nature of the unique excitation wavelength-dependent DS emissions and sensitive excitation power-dependent UC emissions. In a proof-of-concept experiment, the "chameleon-like" NPs are employed as luminescent materials on trademark tag and painting to demonstrate their applications in multilevel anti-counterfeiting.

2 Results and discussion

2.1 Controlled synthesis

The $NaYbF_4$:2%Er core and $NaYbF_4$:2%Er@$NaYF_4$ core/shell NPs were synthesized via a modified Solid-Liquid-Thermal-Decomposition method [32]. Powder X-ray diffraction (XRD) was performed to investigate the phase purity and crystallinity of the synthesized NPs. All of the diffraction peaks of the $NaYbF_4$:2%Er core and $NaYbF_4$:2%Er@$NaYF_4$ core/shell NPs can be well indexed to pure hexagonal $NaYbF_4$ and $NaYF_4$ (JCPDS no. 27-1427 and no. 16-0334), respectively, indicating that the as-prepared samples have good crystallinities without any impurity phase (Fig. S1 in the Electronical Supplementary Material (ESM)). The morphology and size of the $NaYbF_4$:2%Er core and $NaYbF_4$:2%Er@$NaYF_4$ core/shell NPs were characterized by scanning electron microscope (SEM) images (Figs. 1(a) and 1(b)). The as-prepared $NaYbF_4$:2%Er core samples are uniform hexagonal plate with the size of ~ 450 nm × 230 nm. After coating with an inert $NaYF_4$ shell, the as-prepared core/shell NPs remained with the morphology of hexagonal plate, but the size of the NPs increased to be ~ 550 nm × 250 nm. The core/shell structure of $NaYbF_4$:2%Er@$NaYF_4$ NPs can be directly observed from the high-angle annular dark-field scanning TEM (HAADF–STEM) image (Fig. 1(c)). The brighter region corresponds to the heavier Yb^{3+} ions in the core and the darker region corresponds to the lighter Y^{3+} ions in the shell layer. The elemental mapping also reveals that Yb and Y elements are distributed at the core and shell regions (Figs. 1(d)–1(f)), respectively. These characterizations indicate that uniform $NaYbF_4$:2%Er core and $NaYbF_4$:2%Er@$NaYF_4$ core/shell NPs were successfully synthesized.

2.2 Excitation wavelength-dependent DS single-band emissions

As shown in Figs. 2(a) and 2(b), $NaYbF_4$:2%Er NPs exhibit excitation wavelength-dependent single-band red or green emissions upon excitation at 377 or 490 nm, respectively. The proposed mechanisms are shown in Fig. 2(c). In $NaYbF_4$:2%Er NPs, Er^{3+} ions are surrounded by Yb^{3+} ions, so the average distance between Er^{3+} and

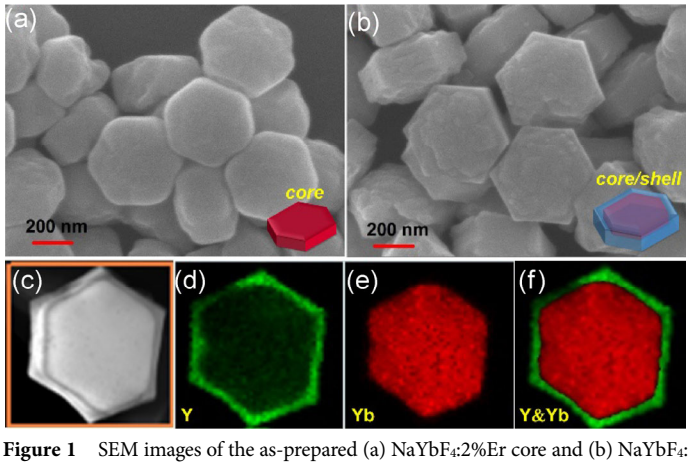

Figure 1 SEM images of the as-prepared (a) $NaYbF_4$:2%Er core and (b) $NaYbF_4$:2%Er@$NaYF_4$ core/shell NPs. (c) HAADF–STEM image and (d)–(f) elemental mapping images of $NaYbF_4$:2%Er@$NaYF_4$ core/shell NPs.

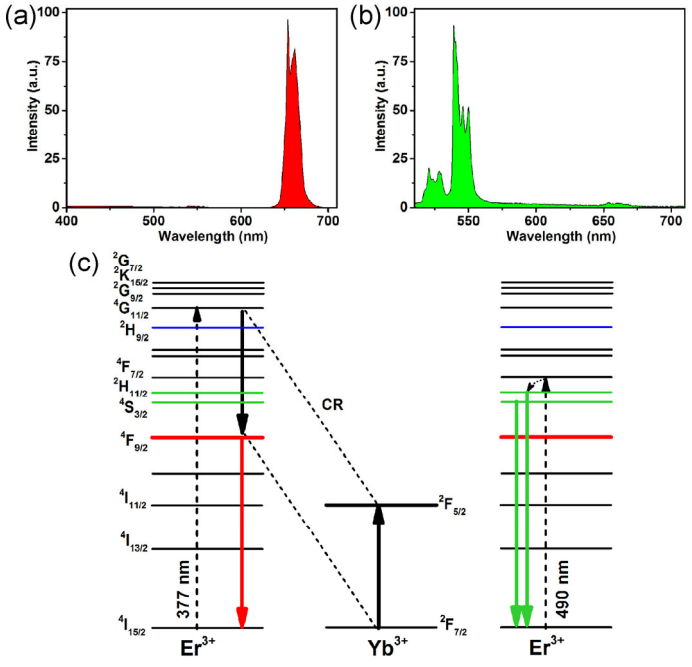

Figure 2 DSL spectra of the $NaYbF_4$:2%Er NPs upon excitation at (a) 377 and (b) 490 nm, respectively. (c) The proposed mechanisms for single-band red and green emissions of Er^{3+} in high Yb^{3+}-doped NPs upon excitation at 377 and 490 nm, respectively.

Yb^{3+} ions is very short. Upon excitation at 377 nm, the electrons of Er^{3+} in the ground state $^4I_{15/2}$ are pumped to $^4G_{11/2}$ by absorbing the incident light. The energy gap between $^4G_{11/2}$ and $^4F_{9/2}$ of Er^{3+} is ~ 11,000 cm^{-1}, which is very close to that between $^2F_{7/2}$ and $^2F_{5/2}$ of Yb^{3+} (~ 10,200 cm^{-1}) [33–36]. Thus, the electrons at $^4G_{11/2}$ may directly relax to $^4F_{9/2}$ due to the cross-relaxation (CR) between Er^{3+} and Yb^{3+}: Er^{3+} ($^4G_{11/2}$) + Yb^{3+} ($^2F_{7/2}$)→Er^{3+} ($^4F_{9/2}$) + Yb^{3+} ($^2F_{5/2}$), rather than stepwise nonradiative relaxation to the lower states ($^2H_{9/2}$, $^4F_{3/2}$, $^4F_{5/2}$, $^4F_{7/2}$, $^2H_{11/2}$, $^4S_{3/2}$, $^4F_{9/2}$…) of Er^{3+} [37]. As a result, no blue emission from $^2H_{9/2}$→$^4I_{15/2}$ and green emission from $^2H_{11/2}/^4S_{3/2}$ → $^4I_{15/2}$ were observed. In this case, almost single-band emission centered at 654 nm ($^4F_{9/2}$→$^4I_{15/2}$) of Er^{3+} was achieved (Fig. 2(b)). By contrast, upon excitation at 490 nm, the electrons in the ground state of Er^{3+} are pumped to the metastable level of $^4F_{7/2}$, followed by fast nonradiative relaxation to the lower excited states of $^2H_{11/2}/^4S_{3/2}$. Multi-phonon nonradiative relaxation from $^2H_{11/2}/^4S_{3/2}$ is negligibly small owing to the large energy gap (~ 3,000 cm^{-1}) between $^2H_{11/2}/^4S_{3/2}$ and the next low-lying $^4F_{9/2}$ of Er^{3+} [36]. Consequently, almost single-band green emission ($^2H_{11/2}/^4S_{3/2}$→$^4I_{15/2}$) was produced (Fig. 2(d)).

In order to confirm our proposed PL mechanisms, a series of $NaYb_xY_{(0.98-x)}F_4$:2%Er (x = 0, 0.2, 0.5, 0.98) NPs were synthesized. Upon excitation at 377 nm, the integrated R/G ratio increased from 0.1 to 116.5 with increasing the doping concentration of Yb^{3+} from 0 to 98% (Fig. 3(a) and Fig. S2 in the ESM). These results indicate that CR between Er^{3+} and Yb^{3+} may be the main reason for the single-band red emission of Er^{3+} ions in high Yb^{3+}-doped NPs. Nevertheless, it was found that all of these $NaYb_xY_{(0.98-x)}F_4$:2%Er NPs displayed very weak red emission upon excitation at 490 nm (Fig. 3(b)). The R/G ratio changed only from 0.11 to 0.07 when the Yb^{3+} doping concentration was increased from 0 to 98% (Fig. S2 in the ESM). The weak red emission verified the low nonradiative relaxation rate from $^2H_{11/2}/^4S_{3/2}$ to $^4F_{9/2}$ in all the Er^{3+} and Yb^{3+} co-doped $NaREF_4$ hosts.

The mechanism of single-band emission can be further confirmed by the excitation spectra of $NaYF_4$:2%Er and $NaYbF_4$:2%Er NPs (Figs. 3(c) and 3(d)). By monitoring the emission of Er^{3+} at 540 and 654 nm, the excitation spectra of $NaYF_4$:2%Er NPs are almost

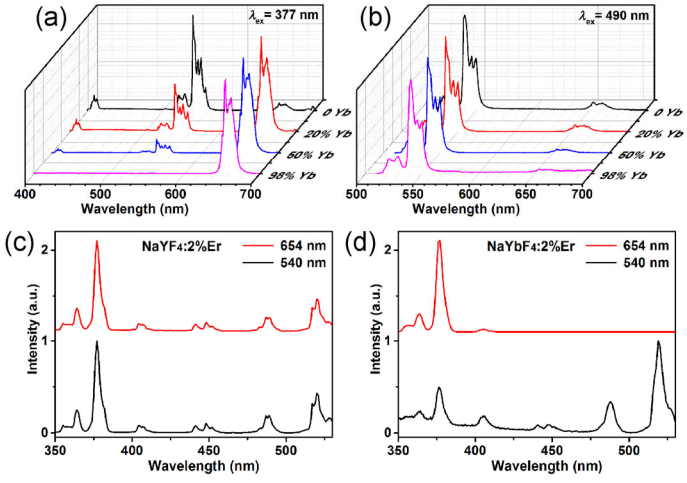

Figure 3 DSL spectra of the $NaYb_xY_{(0.98-x)}F_4$:2%Er (x = 0, 0.2, 0.5, 0.98) NPs upon excitation at (a) 377 and (b) 490 nm, respectively. The excitation spectra of (c) $NaYF_4$:2%Er and (d) $NaYbF_4$:2%Er NPs by monitoring the emission at 654 and 540 nm, respectively.

identical (Fig. 3(c)), which suggests that the green and red emissions are produced through a similar process: nonradiative relaxation from the upper states of Er^{3+} [37]. By contrast, the excitation spectra of $NaYbF_4$:2%Er by monitoring the emission at 540 and 654 nm are markedly different. Specifically, a very strong excitation band centered at 377 nm was observed when monitoring the emission at 654 nm, while a relatively weak band at 377 nm was observed when monitoring the emission at 540 nm (Fig. 3(d)). These results infer that the green and red emissions of $NaYbF_4$:2%Er NPs were achieved via different processes as described above in Fig. 2(c).

2.3 Excitation power-dependent multicolor UC emissions

The efficient energy transfer between Yb^{3+} and Er^{3+} in $NaYbF_4$:2%Er NPs is also in favor of obtaining intense UC emission. In order to further enhance the UC efficiency, we coated the $NaYbF_4$:2%Er NPs with an inert $NaYF_4$ shell layer. The UC emission intensity of the $NaYbF_4$:2%Er@$NaYF_4$ core/shell NPs was enhanced by ~ 4 times as compared to that of $NaYbF_4$:2%Er core-only counterparts under otherwise identical conditions (Fig. S3 in the ESM). Correspondingly, the absolute UCQY was observed to increase from 2.1% to 5.2% after coating with the $NaYF_4$ shell layer. The much stronger UCL intensity in core/shell NPs can be attributed to the protection of an inert $NaYF_4$ shell, which can be verified by the prolonged UCL lifetime of the core/shell NPs (Fig. S3 in the ESM).

Figure 4(a) is the UCL photograph of the $NaYbF_4$:2%Er@$NaYF_4$ core/shell NPs in cyclohexane solution upon excitation with a 980-nm diode laser. Interestingly, the UCL color shows a continuous evolution from red to yellow, and to green along the direction of the laser beam. It is well known that the excitation power density gradually decreases along the direction of the laser beam due to the absorption and the scattering of the NPs in cyclohexane solution. Therefore, the excitation power density played an important role in changing of the UCL color of $NaYbF_4$:2%Er@ $NaYF_4$ core/shell NPs. Hence, we recorded the UC emission spectra at different excitation power density. As shown in Figs. 4(b)–4(d), the $NaYbF_4$:2%Er@$NaYF_4$ core/shell NPs displayed red, yellow and green emissions when the excitation power density was 4.0, 0.5 and 0.1 W/cm^2, respectively. The R/G ratio, which determines the displayed UCL color, was observed to increase from 1.2 to 13.5 when the excitation power density increased from 0.1 to 4.0 W/cm^2 (Fig. 4(e)), but it remained nearly unchanged when further increasing the excitation power density. It implies that both of the UC green and red emissions became saturated when the excitation power density exceeded 4.0 W/cm^2.

Theoretically, the UC emission intensity and the excitation power density should obey the following rule: $I \propto P^n$, where I is the UC emission intensity, P is the excitation power density, and n is the number of photons [38]. For the as-prepared $NaYbF_4$:2%Er@$NaYF_4$ NPs, the measured values of n for green and red emissions are 1.68, 2.28, respectively (Figs. 4(f) and 4(g)). It indicates that the enhancement of the red UCL intensity is much faster than that of the green UCL intensity with increasing the excitation power density. As such, a small change of the excitation power will result in drastic changes of the R/G ratio and UCL color in $NaYbF_4$:2%Er@$NaYF_4$ NPs.

Note that some previous reports indicated that the UCL color of Er^{3+} ions in the low Yb^{3+}-doped fluorides might be insensitive to the excitation power density [39, 40]. For example, the $NaYF_4$:20%Yb,2%Er microcrystals maintained green UC emission under 980 nm laser excitation in the range of 3 × 10^5–6 × 10^5 W/cm^2 [39]. Thus, the concentration of Yb^{3+} ions is one of the key factors for the sensitive excitation power-dependent UC emissions in $NaYbF_4$:2%Er@$NaYF_4$ NPs.

To shed more light on the effect of Yb^{3+} on the UC emissions of Er^{3+}, the UCL spectra of X%Yb,2%Er (X = 20, 50, 98) co-doped $NaYF_4$ NPs upon excitation at different power density (0.1, 0.5 and 4.0 W/cm^2) were recorded (Figs. 4(h)–4(m)). The UCL color of $NaYbF_4$:2%Er core NPs was also observed to be sensitive to the excitation power density and showed a continuous evolution from green to red when increasing the power density from 0.1 to 4.0 W/cm^2 (Figs. 4(h) and 4(k)), which is similar to that of the $NaYbF_4$:2%Er@ $NaYF_4$ core/shell counterparts. However, when the Yb^{3+} concentration decreased from 98% to 50%, the UCL color of the NPs became less sensitive to excitation power density (Figs. 4(i) and 4(l)). Furthermore, when the doping concentration of Yb^{3+} ions decreased to 20%, the UCL color of the NPs became nearly insensitive to excitation power and remained green when increasing the power density from 0.1 to 4.0 W/cm^2 (Figs. 4(j) and 4(m)). The control experiments clearly verify that the higher doped Yb^{3+} concentration facilitates the tailoring of UCL color of Er^{3+} through changing the excitation power density (Fig. S4 in the ESM).

Figures 5(a)–5(c) depict the distribution of lanthanide ions in $NaYF_4$ NPs doped with different concentration of Yb^{3+} (98%, 50%, 20%) ions. It shows that the average distance between Er^{3+} and Yb^{3+} ions decrease with decreasing the concentration of Yb^{3+} ions. The probability of energy transfer (σ) between Er^{3+} and Yb^{3+} ions can be expressed as

$$\sigma = C_{\text{Yb-Er}} \cdot \exp(-2L/R) \quad (1)$$

where L is the distance between Er^{3+} and Yb^{3+}, $C_{\text{Yb-Er}}$ is the Yb-Er interaction constant, and R is the effective Bohr radius [34]. Meanwhile, the absorbed energy (E_{Er}) for single activator of Er^{3+} ions can be expressed as

$$E_{\text{Er}} = \sigma \cdot \eta_{\text{Yb/Er}} \cdot \omega \cdot P \quad (2)$$

where $\eta_{\text{Yb/Er}}$ is the concentration ratio between Yb^{3+} and Er^{3+} ions, ω is the absorption cross-section of Yb^{3+} ions. When increasing the doping concentration of Yb^{3+} ions, the value of σ and $\eta_{\text{Yb/Er}}$ gradually increases. Therefore, the activator of Er^{3+} ions may accept more energy (E_{Er}) from Yb^{3+} ions in the higher Yb^{3+}-doped host, resulting in an increase in the electronic population of the upper states of Er^{3+} ions.

The proposed UC mechanisms are shown in Fig. 5(d). Upon excitation at 980 nm, Yb^{3+} ions act as sensitizers to absorb the energy and then transfer it to the nearby Er^{3+} ions. The electrons at ground state of Er^{3+} can be excited to $^4F_{7/2}$ via two-photon UC process, followed by nonradiative relaxation to $^2H_{11/2}/^4S_{3/2}$. It has been reported that there are two kinds of transition paths for the electrons at the $^2H_{11/2}/^4S_{3/2}$ [41]. One path (path A) is radiative

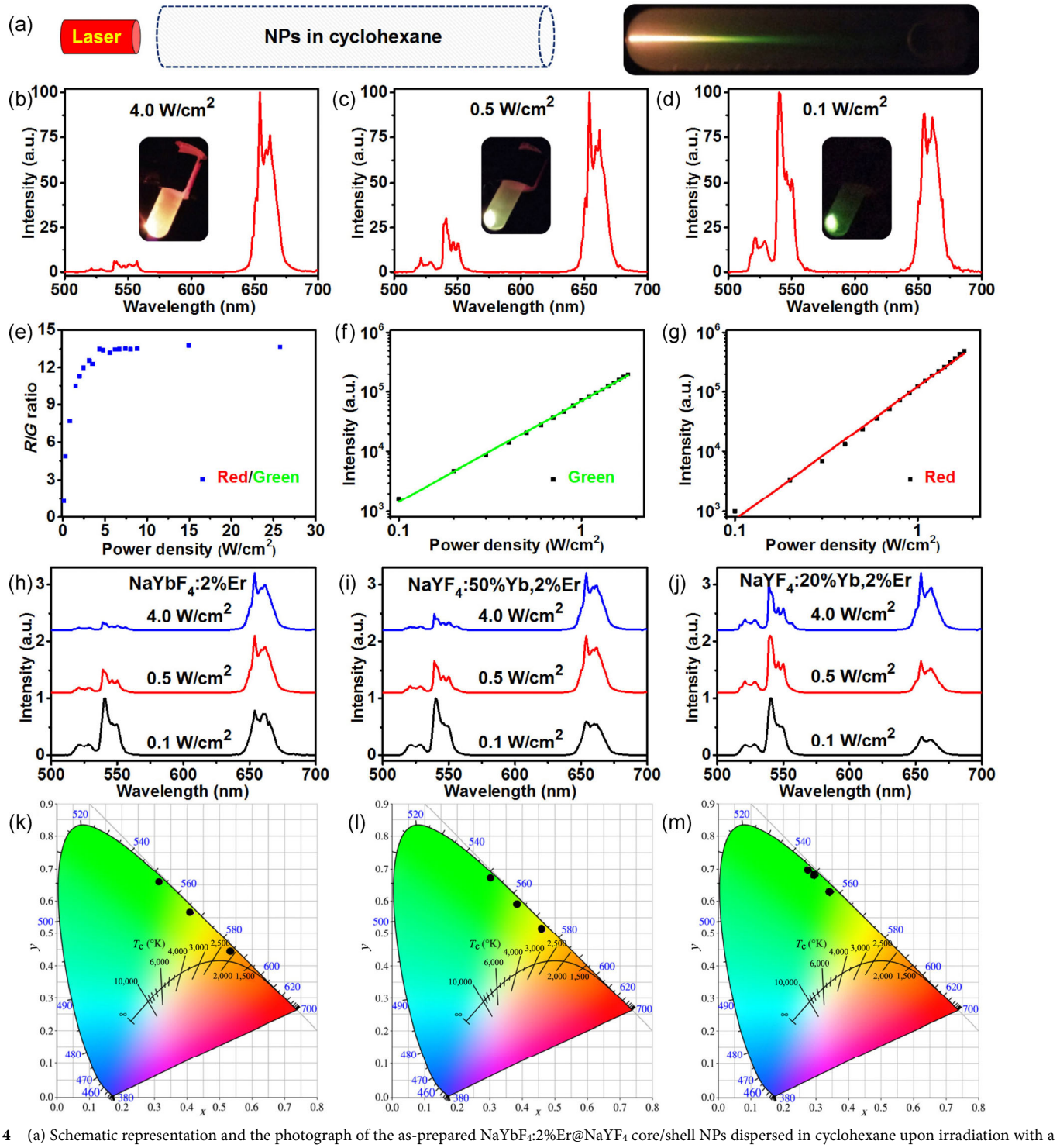

Figure 4 (a) Schematic representation and the photograph of the as-prepared $NaYbF_4$:2%Er@$NaYF_4$ core/shell NPs dispersed in cyclohexane upon irradiation with a 980-nm diode laser. UCL spectra and the corresponding photos of the $NaYbF_4$:2%Er@$NaYF_4$ core/shell NPs with the excitation power density of (b) 0.1, (c) 0.5 and (d) 4.0 W/cm^2, respectively. (e) The *R*/*G* ratio at different excitation power density. Log–log plot of the UC (f) red and (g) green emission intensity of the $NaYbF_4$:2%Er@$NaYF_4$ core/shell NPs as a function of the pump power density of 980 nm. (h)–(j) UCL spectra and (k)–(m) corresponding CIE chromaticity coordinates of the *X*%Yb,2%Er (*X* = 98, 50, 20) doped $NaYF_4$ NPs upon 980 nm laser excitation with power density of 0.1, 0.5, 4.0 W/cm^2, respectively.

relaxation to the ground state, resulting in green emission. The other (path B) is pumping to the $^{2,4}G_J/^2K_{15}$ via three-photon UC process, followed by nonradiative relaxation to $^4G_{11/2}$. Note that both paths compete with each other. When the excitation power density is relatively low, path A will be dominant. Thus, both the high and low Yb^{3+}-doped NPs display green UC emission. Upon further increasing the excitation power, path B tends to predominate in the emission process of Er^{3+}. In high Yb^{3+}-doped NPs, the electrons at $^4G_{11/2}$ may directly relax to $^4F_{9/2}$ via the CR process between Er^{3+} and Yb^{3+}: Er^{3+} ($^4G_{11/2}$) + Yb^{3+} ($^2F_{7/2}$) → Er^{3+} ($^4F_{9/2}$) + Yb^{3+} ($^2F_{5/2}$), leading to the UC red emission [41]. Hence, the *R*/*G* ratio rapidly increased and the corresponding UCL color markedly changed with increasing the excitation power. By contrast, the *R*/*G* ratio and UCL color of Er^{3+} showed no obvious change with increasing the excitation power in low Yb^{3+}-doped NPs (Fig. 4(m)), due mainly to the low CR rate between Yb^{3+} and Er^{3+} ions. As a result, most of the electrons of Er^{3+} at the upper state of $^4G_{11/2}$ may gradually relax to the $^2H_{11/2}/^4S_{3/2}$, giving rise to the green emissions (Fig. 5(d)).

To the best of our knowledge, such sensitive excitation power-

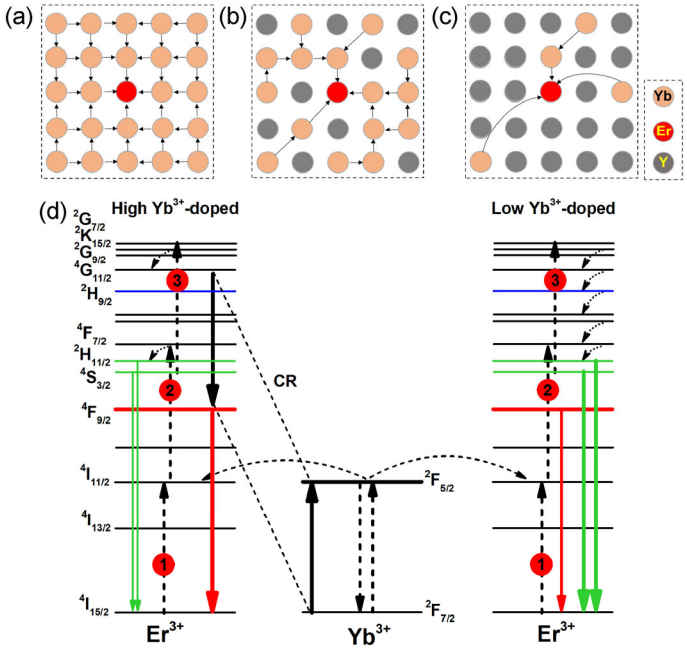

Figure 5 (a)–(c) Schematic illustration of the lanthanide ions distribution in different concentration of Yb^{3+} (98%, 50%, 20%) doped $NaYF_4$ NPs. (d) The proposed mechanisms for UC red and green emissions of Er^{3+} in high and low Yb^{3+}-doped $NaYF_4$, respectively.

dependent UC emissions and excitation wavelength-dependent DS single-band emissions had never been achieved before in one and the same material. Even in other high Yb^{3+}-doped inorganic luminescent materials like $LiYbF_4$:2%Er@$LiYF_4$ NCs, the UCL color of Er^{3+} was observed to be insensitive to excitation power density and ordinary multi-band emissions were afforded upon excitation at either 377 or 490 nm (Fig. S5 in the ESM). This phenomenon might be closely related to the crystal structure. Based on the cell parameters, the nearest distance between Er^{3+} and Yb^{3+} in $LiYbF_4$:2%Er is determined to be 3.687 Å, which is longer than that (3.496 Å) in $NaYbF_4$:2%Er [42, 43]. Consequently, the CR rate between Er^{3+} and Yb^{3+} in $LiYbF_4$:2%Er should be lower than that in $NaYbF_4$:2%Er according to Eq. (1).

2.4 Multilevel anti-counterfeiting applications

The tunable multicolor luminescence of the $NaYbF_4$:2%Er@$NaYF_4$ NPs offers great opportunities for multilevel anti-counterfeiting applications. As a proof-of-concept experiment, we prepared the security label by coating the $NaYbF_4$:2%Er@$NaYF_4$ NPs onto the non-fluorescence trademark tag (Fig. 6(a)). Thanks to the high UCL efficiency and sensitive excitation power-dependent UC emissions of the $NaYbF_4$:2%Er@$NaYF_4$ NPs, a cheap (~ 10 $) 980-nm laser diode with the power of ~ 100 mW can be used as light source to guarantee an adequate anti-counterfeiting effect. The irradiation power density on the security label and the corresponding UCL color can be easily tuned by changing the distance between the laser and security label. The color evolution can be easily recognized and distinguished by naked eyes (Fig. 6(a)). Meanwhile, the security label also showed single-band red and green emissions upon excitation at 377 and 490 nm, respectively. In comparison with the multi-band emissions from traditional lanthanide-based anti-counterfeiting materials, the unique excitation wavelength-dependent DS single-band emissions in the prototype security label can significantly improve the anti-counterfeiting ability.

Furthermore, we employed the lanthanide-doped fluoride NPs as security inks on a painting, where $NaYbF_4$:2%Er@$NaYF_4$ and $NaYF_4$:20%Yb,2%Er were painted on the apple and leaf, respectively (Fig. 6(b)). Upon increasing the excitation power density, the apple

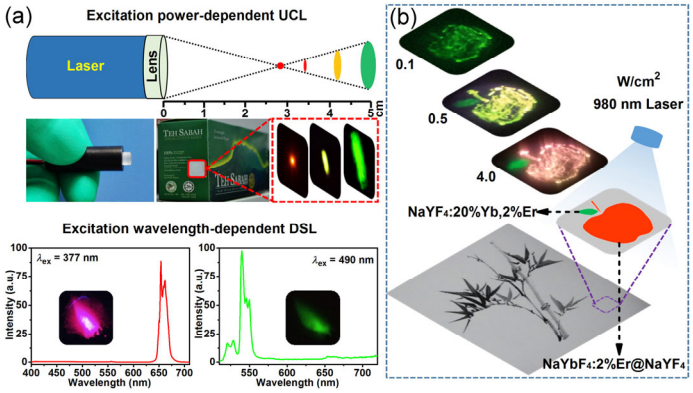

Figure 6 Multilevel anti-counterfeit applications of the $NaYbF_4$:2%Er@$NaYF_4$ NPs. (a) The security label coated with $NaYbF_4$:2%Er@$NaYF_4$ NPs for UCL/DSL multilevel anti-counterfeiting application. (b) The $NaYbF_4$:2%Er@$NaYF_4$ NPs and $NaYF_4$:20%Yb,2%Er NPs were employed as security inks on a painting.

displayed a continuous evolution color from green, to yellow, and to red. Instead, the leaf of the apple pattern remained with weak green emissions, since the UCL spectra of $NaYF_4$:20%Yb,2%Er NPs are insensitive to the excitation power density. These results demonstrate the superiority and irreplaceability of $NaYbF_4$:2%Er@$NaYF_4$ NPs in multilevel anti-counterfeiting fields.

3 Conclusions

In summary, we have explored a novel class of multilevel anti-counterfeiting materials based on $NaYbF_4$:2%Er@$NaYF_4$ core/shell NPs, which bring together the advantages of single-band DS emissions and multicolor tunable UC emissions in one and the same material. Unlike conventional single-level anti-counterfeiting materials that display nearly unaltered emission color, the proposed NPs with excitation wavelength- and power-responsive color evolution are favorable for recognition by naked eyes and difficult to be imitated by counterfeiters with other luminescent materials, allowing their potential multilevel anti-counterfeiting applications in a variety of fields such as paper money, packaging, artwork, valuable documents, and certificates.

Acknowledgements

This work is supported by the National Natural Foundation of China (NSFC) (Nos. 21771185, 51672272, 21650110462, and U1805252), the Strategic Priority Research Program of the CAS (No. XDB20000000), the CAS/SAFEA International Partnership Program for Creative Research Teams, and Natural Science Foundation of Fujian Province (No. 2017I0018).

Electronic Supplementary Material: Supplementary material (experimental details, powder XRD patterns of the as-prepared $NaYbF_4$:2%Er core and $NaYbF_4$:2%Er@$NaYF_4$ core/shell NPs, *R*/*G* ratio for $NaYb_xY_{(0.98-x)}F_4$:2%Er (x = 0, 0.2, 0.5, 0.98) NPs upon excitation at different wavelengths, UCL spectra and UCL decays of the $NaYbF_4$:2%Er core and $NaYbF_4$:2%Er@$NaYF_4$ core/shell NPs, powder XRD pattern, TEM image and UCL/DSL spectra of the $LiYbF_4$:2%Er@$LiYF_4$ core/shell NPs) is available in the online version of this article at https://doi.org/10.1007/s12274-019-2366-z.

References

[1] Kumar, P.; Singh, S.; Gupta, B. K. Future prospects of luminescent nanomaterial based security inks: From synthesis to anti-counterfeiting applications. *Nanoscale* **2016**, *8*, 14297–14340.

[2] Liu, Y. L.; Ai, K. L.; Lu, L. H. Designing lanthanide-doped nanocrystals with both up- and down-conversion luminescence for anti-counterfeiting.

Nanoscale **2011**, *3*, 4804–4810.
[3] Kaczmarek, A. M.; Liu, Y. Y.; Wang, C. H.; Laforce, B.; Vincze, L.; Van Der Voort, P.; Van Hecke, K.; Van Deun, R. Lanthanide "chameleon" multistage anti-counterfeit materials. *Adv. Funct. Mater.* **2017**, *27*, 1700258.
[4] Zhang, Y. H.; Zhang, L. X.; Deng, R. R.; Tian, J.; Zong, Y.; Jin, D. Y.; Liu, X. G. Multicolor barcoding in a single upconversion crystal. *J. Am. Chem. Soc.* **2014**, *136*, 4893–4896.
[5] Wang, F.; Liu, X. G. Multicolor tuning of lanthanide-doped nanoparticles by single wavelength excitation. *Acc. Chem. Res.* **2014**, *47*, 1378–1385.
[6] Dong, H.; Du, S. R.; Zheng, X. Y.; Lyu, G. M.; Sun, L. D.; Li, L. D.; Zhang, P. Z.; Zhang, C.; Yan, C. H. Lanthanide nanoparticles: From design toward bioimaging and therapy. *Chem. Rev.* **2015**, *115*, 10725–10815.
[7] Zheng, W.; Huang, P.; Tu, D. T.; Ma, E.; Zhu, H. M.; Chen, X. Y. Lanthanide-doped upconversion nano-bioprobes: Electronic structures, optical properties, and biodetection. *Chem. Soc. Rev.* **2015**, *44*, 1379–1415.
[8] Wang, Y.; Zheng, K. Z.; Song, S. Y.; Fan, D. Y.; Zhang, H. J.; Liu, X. G. Remote manipulation of upconversion luminescence. *Chem. Soc. Rev.* **2018**, *47*, 6473–6485.
[9] Zhao, J. B.; Jin, D. Y.; Schartner, E. P.; Lu, Y. Q.; Liu, Y. J.; Zvyagin, A. V.; Zhang, L. X.; Dawes, J. M.; Xi, P.; Piper, J. A. et al. Single-nanocrystal sensitivity achieved by enhanced upconversion luminescence. *Nat. Nanotechnol.* **2013**, *8*, 729–734.
[10] Liu, Y. S.; Tu, D. T.; Zhu, H. M.; Li, R. F.; Luo, W. Q.; Chen, X. Y. A strategy to achieve efficient dual-mode luminescence of Eu^{3+} in lanthanides doped multifunctional $NaGdF_4$ nanocrystals. *Adv. Mater.* **2010**, *22*, 3266–3271.
[11] Tu, D. T.; Zheng, W.; Huang, P.; Chen, X. Y. Europium-activated luminescent nanoprobes: From fundamentals to bioapplications. *Coordin. Chem. Rev.* **2019**, *378*, 104–120.
[12] Bünzli, J. C. G. Benefiting from the unique properties of lanthanide ions. *Acc. Chem. Res.* **2006**, *39*, 53–61.
[13] Peng, D. F.; Ju, Q.; Chen, X.; Ma, R. H.; Chen, B.; Bai, G. X.; Hao, J. H.; Qiao, X. S.; Fan, X. P.; Wang, F. Lanthanide-doped energy cascade nanoparticles: Full spectrum emission by single wavelength excitation. *Chem. Mater.* **2015**, *27*, 3115–3120.
[14] Tan, M. L.; Del Rosal, B.; Zhang, Y. Q.; Martín Rodríguez, E.; Hu, J.; Zhou, Z. G.; Fan, R. W.; Ortgies, D. H.; Fernández, N.; Chaves-Coira, I. et al. Rare-earth-doped fluoride nanoparticles with engineered long luminescence lifetime for time-gated *in vivo* optical imaging in the second biological window. *Nanoscale* **2018**, *10*, 17771–17780.
[15] Kraft, M.; Würth, C.; Muhr, V.; Hirsch, T.; Resch-Genger, U. Particle-size-dependent upconversion luminescence of $NaYF_4$: Yb, Er nanoparticles in organic solvents and water at different excitation power densities. *Nano Res.* **2018**, *11*, 6360–6374.
[16] Li, L.Y.; Zhao, N. J.; Fu, L. M.; Zhou, J.; Ai, X. C.; Zhang, J. P. Temperature modulation of concentration quenching in lanthanide-doped nanoparticles for enhanced upconversion luminescence. *Nano Res.* **2018**, *11*, 2104–2115.
[17] Li, Y. F.; Zhang, Y. M.; Wang, W. P. Phototriggered targeting of nanocarriers for drug delivery. *Nano Res.* **2018**, *11*, 5424–5438.
[18] Liu, Y.; Tu, D. T.; Zheng, W.; Lu, L. Y.; You, W. W.; Zhou, S. Y.; Huang, P.; Li, R. F.; Chen, X. Y. A strategy for accurate detection of glucose in human serum and whole blood based on an upconversion nanoparticles-polydopamine nanosystem. *Nano Res.* **2018**, *11*, 3164–3174.
[19] Wang, Y. Q.; Wang, J.; Ma, Q. Q.; Li, Z. H.; Yuan, Q. Recent progress in background-free latent fingerprint imaging. *Nano Res.* **2018**, *11*, 5499–5518.
[20] Jung, T.; Jo, H. L.; Nam, S. H.; Yoo, B.; Cho, Y.; Kim, J.; Kim, H. M.; Hyeon, T.; Suh, Y. D.; Lee, H. et al. The preferred upconversion pathway for the red emission of lanthanide-doped upconverting nanoparticles, $NaYF_4$:Yb^{3+},E^{3+}. *Phys. Chem. Chem. Phys.* **2015**, *17*, 13201–13205.
[21] Tang, Z. J.; Liu, Q.; Li, J.; Wu, X. F.; Zhan, S. P.; Nie, G. Z.; Hu, J. S.; Hu, S. G.; Xi, Z. F.; Wu, S. B. et al. Tuning the photothermal effect of $NaYF_4$: Yb^{3+}, Er^{3+} upconversion luminescent crystals through La^{3+} ion doping. *J. Lumin.* **2019**, *206*, 21–26.
[22] Xu, J. T.; Yang, P. P.; Sun, M. D.; Bi, H. T.; Liu, B.; Yang, D.; Gai, S. L.; He, F.; Lin, J. Highly emissive dye-sensitized upconversion nanostructure for dual-photosensitizer photodynamic therapy and bioimaging. *ACS Nano* **2017**, *11*, 4133–4144.
[23] You, W. W.; Tu, D. T.; Zheng, W.; Huang, P.; Chen, X. Y. Lanthanide-doped disordered crystals: Site symmetry and optical properties. *J. Lumin.* **2018**, *201*, 255–264.
[24] Yang, D. M.; Ma, P. A.; Hou, Z. Y.; Cheng, Z. Y.; Li, C. X.; Lin, J. Current advances in lanthanide ion (Ln^{3+})-based upconversion nanomaterials for drug delivery. *Chem. Soc. Rev.* **2015**, *44*, 1416–1448.
[25] Gai, S. L.; Li, C. X.; Yang, P. P.; Lin, J. Recent progress in rare earth micro/nanocrystals: Soft chemical synthesis, luminescent properties, and biomedical applications. *Chem. Rev.* **2014**, *114*, 2343–2389.
[26] Dai, Y. L.; Xiao, H. H.; Liu, J. H.; Yuan, Q. H.; Ma, P. A.; Yang, D. M.; Li, C. X.; Cheng, Z. Y.; Hou, Z. Y.; Yang, P. P. et al. *In vivo* multimodality imaging and cancer therapy by near-infrared light-triggered trans-platinum pro-drug-conjugated upconverison nanoparticles. *J. Am. Chem. Soc.* **2013**, *135*, 18920–18929.
[27] Zhang, C.; Yang, L.; Zhao, J.; Liu, B. H.; Han, M. Y.; Zhang, Z. P. White-light emission from an integrated upconversion nanostructure: Toward multicolor displays modulated by laser power. *Angew. Chem., Int. Ed.* **2015**, *54*, 11531–11535.
[28] Chen, B.; Liu, Y.; Xiao, Y.; Chen, X.; Li, Y.; Li, M. Y.; Qiao, X. S.; Fan, X. P.; Wang, F. Amplifying excitation-power sensitivity of photon upconversion in a $NaYbF_4$:Ho nanostructure for direct visualization of electromagnetic hotspots. *J. Phys. Chem. Lett.* **2016**, *7*, 4916–4921.
[29] Liu, J.; Rijckaert, H.; Zeng, M.; Haustraete, K.; Laforce, B.; Vincze, L.; Van Driessche, I.; Kaczmarek, A. M.; Van Deun, R. Simultaneously excited downshifting/upconversion luminescence from lanthanide-doped core/shell fluoride nanoparticles for multimode anticounterfeiting. *Adv. Funct. Mater.* **2018**, *28*, 1707365.
[30] Schäfer, H.; Ptacek, P.; Voss, B.; Eickmeier, H.; Nordmann, J; Haase, M. Synthesis and characterization of upconversion fluorescent Yb^{3+}, Er^{3+} doped RbY_2F_7 nano- and microcrystals. *Cryst. Growth Des.* **2010**, *10*, 2202–2208.
[31] Ju, Q.; Tu, D. T.; Liu, Y. S.; Li, R. F.; Zhu, H. M.; Chen, J. C.; Chen, Z.; Huang, M. D.; Chen, X. Y. Amine-functionalized lanthanide-doped $KGdF_4$ nanocrystals as potential optical/magnetic multimodal bioprobes. *J. Am. Chem. Soc.* **2012**, *134*, 1323–1330.
[32] You, W. W.; Tu, D. T.; Zheng, W.; Shang, X. Y.; Song, X. R.; Zhou, S. Y.; Liu, Y.; Li, R. F.; Chen, X. Y. Large-scale synthesis of uniform lanthanide-doped $NaREF_4$ upconversion/downshifting nanoprobes for bioapplications. *Nanoscale* **2018**, *10*, 11477–11484.
[33] Ma, C. G.; Brik, M. G.; Liu, D. X.; Feng, B.; Tian, Y.; Suchocki, A. Energy level schemes of f^N electronic configurations for the di-, tri-, and tetravalent lanthanides and actinides in a free state. *J. Lumin.* **2016**, *170*, 369–374.
[34] Wang, J.; Deng, R. R.; MacDonald, M. A.; Chen, B. L.; Yuan, J. K.; Wang, F.; Chi, D. Z.; Hor, T. S. A.; Zhang, P.; Liu, G. K. et al. Enhancing multiphoton upconversion through energy clustering at sublattice level. *Nat. Mater.* **2014**, *13*, 157–162.
[35] Wang, L. L.; Xue, X. J.; Chen, H.; Zhao, D.; Qin, W. P.. Unusual radiative transitions of Eu^{3+} ions in Yb/Er/Eu tri-doped $NaYF_4$ nanocrystals under infrared excitation. *Chem. Phys. Lett.* **2010**, *485*, 183–186.
[36] Chen, X. Y.; Ma, E.; Liu, G. K. Energy levels and optical spectroscopy of Er^{3+} in Gd_2O_3 nanocrystals. *J. Phys. Chem. C* **2007**, *111*, 10404–10411.
[37] Aarts, L.; van der Ende, B. M.; Meijerink, A. Downconversion for solar cells in $NaYF_4$:Er,Yb. *J. Appl. Phys.* **2009**, *106*, 023522.
[38] Pollnau, M.; Gamelin, D. R.; Lüthi, S. R.; Güdel, H. U.; Hehlen, M. P. Power dependence of upconversion luminescence in lanthanide and transition-metal-ion systems. *Phys. Rev. B* **2000**, *61*, 3337–3346.
[39] Fan, S. H.; Wang, S. K.; Yu, L.; Sun, H. T.; Gao, G. J.; Hu, L. L. Ion-redistribution induced efficient upconversion in β-$NaYF_4$:20%Yb^{3+},2%Er^{3+} microcrystals with well controlled morphology and size. *Opt. Express* **2017**, *25*, 180–190.
[40] Wang, T.; Yu, H.; Siu, C. K.; Qiu, J. B.; Xu, X. H.; Yu, S. F. White-light whispering-gallery-mode lasing from lanthanide-doped upconversion $NaYF_4$ hexagonal microrods. *ACS Photonics* **2017**, *4*, 1539–1543.
[41] Berry, M. T.; May, P. S. Disputed mechanism for NIR-to-red upconversion luminescence in $NaYF_4$:Yb^{3+},Er^{3+}. *J. Phys. Chem. A* **2015**, *119*, 9805–9811.
[42] Shao, W.; Lim, C. K.; Li, Q.; Swihart, M. T.; Prasad, P. N. Dramatic enhancement of quantum cutting in lanthanide-doped nanocrystals photosensitized with an aggregation-induced enhanced emission dye. *Nano Lett.* **2018**, *18*, 4922–4926.
[43] Thoma, R. E.; Brunton, G. D.; Penneman, R. A.; Keenan, T. K. Equilibrium relations and crystal structure of lithium fluorolanthanate phases. *Inorg. Chem.* **1970**, *9*, 1096–1101.